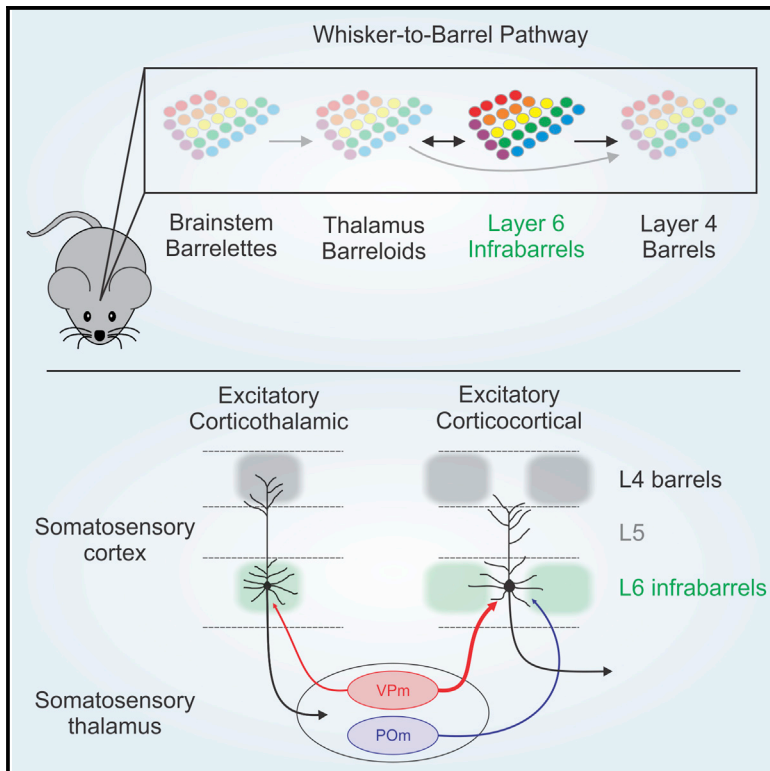


Infrabarrels Are Layer 6 Circuit Modules in the Barrel Cortex that Link Long-Range Inputs and Outputs

Graphical Abstract



Authors

Shane R. Crandall, Sandra L. Patrick,
Scott J. Cruikshank, Barry W. Connors

Correspondence

cranda86@msu.edu

In Brief

Layer 6 is a major input-output layer of neocortex, but key principles of its circuit organization are lacking. Crandall et al. reveal barrel-like structures called infrabarrels that include distinct excitatory circuits linking thalamic inputs with specific outputs, thus providing a framework for understanding the functional organization of layer 6.

Highlights

- Layer 6a of the somatosensory cortex has barrel-like structures called infrabarrels
- Corticothalamic cells group within and corticocortical cells between infrabarrels
- Inputs from somatosensory thalamus selectively target these two neuron types
- Synaptic and intrinsic properties control corticothalamic responses to thalamic input



Infrabarrels Are Layer 6 Circuit Modules in the Barrel Cortex that Link Long-Range Inputs and Outputs

Shane R. Crandall,^{1,2,3,*} Sandra L. Patrick,¹ Scott J. Cruikshank,¹ and Barry W. Connors¹

¹Department of Neuroscience, Division of Biology and Medicine, Brown University, Providence, RI 02912, USA

²Present address: Department of Physiology, Michigan State University, East Lansing, MI 48824, USA

³Lead Contact

*Correspondence: cranda86@msu.edu

<https://doi.org/10.1016/j.celrep.2017.11.049>

SUMMARY

The rodent somatosensory cortex includes well-defined examples of cortical columns—the barrel columns—that extend throughout the cortical depth and are defined by discrete clusters of neurons in layer 4 (L4) called barrels. Using the cell-type-specific *Ntsr1-Cre* mouse line, we found that L6 contains infrabarrels, readily identifiable units that align with the L4 barrels. Corticothalamic (CT) neurons and their local axons cluster within the infrabarrels, whereas corticocortical (CC) neurons are densest between infrabarrels. Optogenetic experiments showed that CC cells received robust input from somatosensory thalamic nuclei, whereas CT cells received much weaker thalamic inputs. We also found that CT neurons are intrinsically less excitable, revealing that both synaptic and intrinsic mechanisms contribute to the low firing rates of CT neurons often reported *in vivo*. In summary, infrabarrels are discrete cortical circuit modules containing two partially separated excitatory networks that link long-distance thalamic inputs with specific outputs.

INTRODUCTION

Vertically organized circuits are a hallmark of the mammalian neocortex (Lorente de Nó, 1938). The discovery that neurons with similar functional properties tend to extend vertically across the layers of sensory neocortex inspired the hypothesis that columns are the elementary unit of neocortical organization (Mountcastle, 1957). Cortical columns have since been observed across a wide variety of neocortical areas and species (Mountcastle, 1997). Structurally, columns consist of ensembles of distinct neuronal subtypes that make dense, vertically oriented connections across all layers (Douglas and Martin, 2004; Harris and Shepherd, 2015; Lefort et al., 2009). Each layer is further defined by specific long-range inputs and outputs (Douglas and Martin, 2004; Harris and Shepherd, 2015; Herkenham, 1980; Lefort et al., 2009). While the definition and functions of cortical columns are a matter of spirited

debate (Horton and Adams, 2005), it has been a valuable concept for understanding the functional organization of the neocortex (Mountcastle, 1997).

One of the clearest examples of columnar organization is found in the vibrissa representation of rodent primary somatosensory (S1) cortex, a leading model for the study of neocortical circuits, sensory processing, development, and plasticity (Andermann and Moore, 2006; Diamond et al., 2008; Feldman and Brecht, 2005; Feldmeyer et al., 2013; Fox, 2008). Here discrete clusters of neurons in layer 4 (L4), called barrels, correlate one to one with the vibrissae on the snout (Simons, 1978; Woolsey and Van der Loos, 1970). Separating each L4 barrel are neuron-sparse septa. Because neurons above and below barrels respond best to one vibrissa (Simons, 1978), the L4 barrel also defines the dimensions of a barrel column, a cytoarchitectonic equivalent of the cortical column. On the basis of anatomical and physiological data (Alloway et al., 2004; Kerr et al., 2007; Kim and Ebner, 1999; Lu and Lin, 1993; Shepherd and Svoboda, 2005), it has been proposed that barrel columns and their surrounding septa comprise distinct excitatory circuits (Alloway, 2008). The links between barrel columns and septa and their functional organization within each layer are still poorly understood.

Perhaps the most enigmatic layer of the neocortex is its deepest, layer 6 (L6) (Briggs, 2010; Thomson, 2010). Neocortical L6 is a principal output layer that has an essential role in modulating both cortical and thalamic activities (Crandall et al., 2015; Denman and Contreras, 2015; Guo et al., 2017; Kim et al., 2014; Lam and Sherman, 2010; Li and Ebner, 2007; Mease et al., 2014; Olsen et al., 2012; Temereanca and Simons, 2004). L6 neurons receive direct input from excitatory thalamic relay neurons (Beierlein and Connors, 2002; Constantinople and Bruno, 2013; Cruikshank et al., 2010; Oberlaender et al., 2012; Yang et al., 2014), implying that L6 may play a strategic role in early thalamocortical processing. Among all the cortical layers, L6 also contains the richest diversity of morphologically and physiologically distinct neurons (Briggs, 2010; Briggs et al., 2016; Chen et al., 2009; Kumar and Ohana, 2008; Thomson, 2010; Zhang and Deschênes, 1997). This heterogeneity has made L6 difficult to study. Broadly speaking, three main types of L6 neurons can be defined by their axonal projections (Zhang and Deschênes, 1997): excitatory corticothalamic (CT) and corticocortical (CC) projection neurons and local inhibitory interneurons. The L6 projection neurons differ in their intrinsic properties,



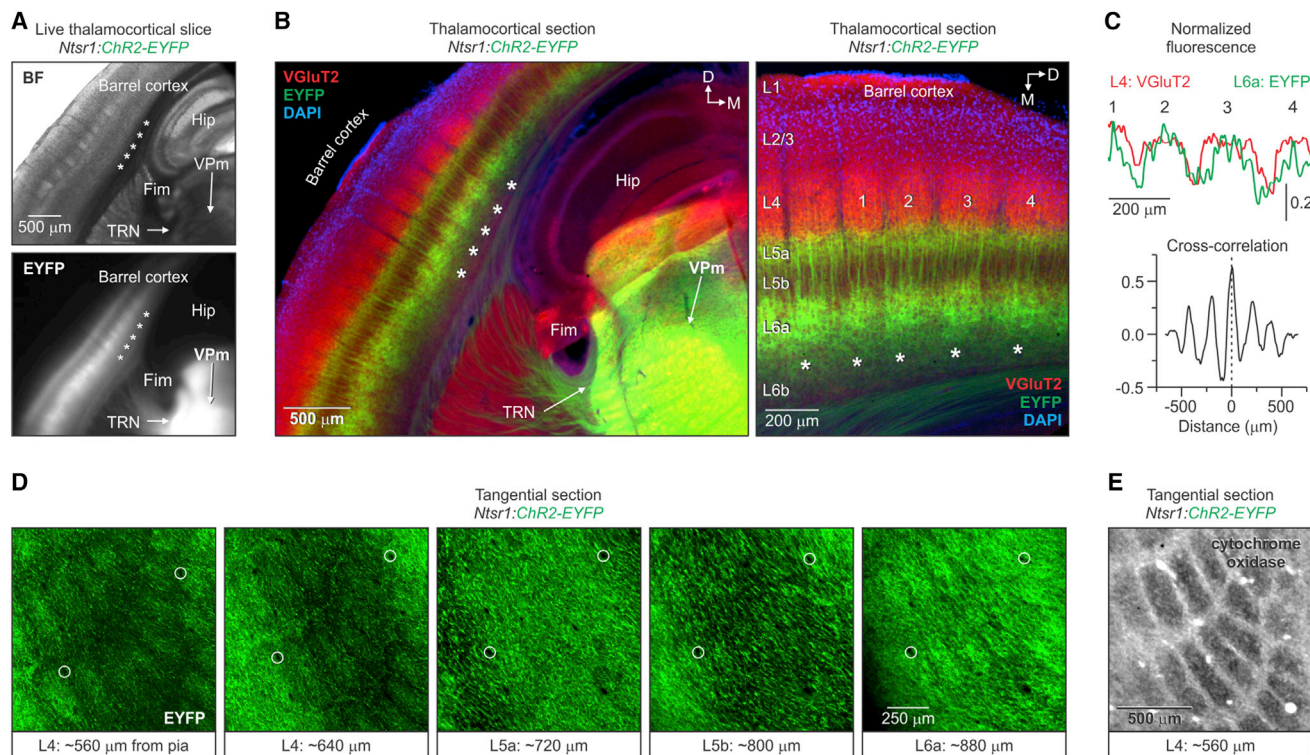


Figure 1. Infrabarrels in L6a of the Primary Somatosensory Cortex

(A) (Top) Bright-field (BF) image of a live 300- μ m-thick thalamocortical slice through the barrel cortex of a 25-day-old *Ntsr1:ChR2-EYFP* mouse. (Bottom) Epi-fluorescence image of the same slice shows a periodic pattern of EYFP in infragranular layers (asterisks) (similar patterns were observed in $n > 27$ mice). (B) (Left) Image of an 80- μ m-thick section, obtained from the slice shown in (A), stained immunohistochemically for VGluT2 and DAPI. (Right) Higher magnification image shows the relationship between VGluT2 and EYFP fluorescence. (C) Cross-correlation of the fluorescence intensity profiles (L4, VGluT2; L6a, EYFP) as a function of horizontal distance for the 4 barrels labeled in (B). EYFP fluorescence in L6a was strongly correlated with the L4 VGluT2 fluorescence (mean peak correlation = 0.50 ± 0.04 ; $n = 7$ slices, 7 hemispheres, and 6 mice). (D) Confocal images of adjacent 80- μ m-thick tangential sections through the barrel cortex of a 26-day-old *Ntsr1:ChR2-EYFP* mouse. Notice the row-like pattern of ellipsoid-shaped EYFP units in L4 and L6a. Sections were aligned by blood vessels (circles) (similar patterns were observed in 4 hemispheres from 2 mice). (E) A cytochrome oxidase-stained tangential section through L4 of the barrel cortex. Tissue was obtained from the opposite hemisphere of the mouse shown in (D) ($n = 2$ hemispheres from 2 mice). Hip, hippocampus; Fim, fimbria; TRN, thalamic reticular nucleus; VPm, ventral posterior medial nucleus. See also Figure S1.

dendrite and axon morphologies, long-range inputs and outputs, and *in vivo* activity patterns (Kumar and Ohana, 2008; Narayanan et al., 2015; Oberlaender et al., 2012; Vélez-Fort et al., 2014; Yang et al., 2014); this has led to suggestions that L6 CT and CC cells participate in distinct subcircuits within the infragranular network (Kumar and Ohana, 2008; Vélez-Fort et al., 2014).

To clarify our understanding of distinct L6 neuronal classes, we turned to cell-type-specific genetics. Here we used the *Ntsr1-Cre* mouse line, which selectively expresses Cre recombinase in L6 CT neurons (Bortone et al., 2014; Crandall et al., 2015; Kim et al., 2014; Olsen et al., 2012), and other Cre lines to achieve cell-type-specific expression of reporters for reliable identification in an *in vitro* preparation of mouse somatosensory forebrain (Agmon and Connors, 1991). These techniques revealed a cortical circuit module, the L6 infrabarrel, that is delineated by differential clustering of CT and CC neurons. Specific photostimulation of thalamocortical pathways (Cruikshank et al., 2010) showed that infrabarrel circuits link distinct long-range inputs with two different L6 output streams.

RESULTS

Infrabarrels in L6a of Mouse Primary Somatosensory Cortex

To explore the organization of L6 in the barrel cortex, we first examined the fluorescence of live brain slices prepared from mice in which a channelrhodopsin-2/enhanced yellow fluorescent protein (ChR2-EYFP) reporter line (Ai32) was crossed to the *Ntsr1-Cre* line, known to label L6 CT cells selectively (Bortone et al., 2014; Crandall et al., 2015; Kim et al., 2014; Olsen et al., 2012). The transgenic approach allowed us to analyze the L6 CT cell population without the variable expression patterns inherent to viral methods. We routinely observed a periodic pattern of EYFP fluorescence in infragranular layers of the barrel cortex that resembled the L4 barrels seen under bright-field illumination (Figure 1A). This EYFP pattern was seen in a variety of slice planes and across a range of ages (15–64 postnatal days old) (Figure S1).

Next, we analyzed the characteristics of the EYFP pattern in fixed tissue immunostained for vesicular glutamate transporter

2 (VGLuT2), which labels the presynaptic terminals of thalamocortical axons and sharply delineates L4 barrels. The discrete, periodic pattern of EYFP was specific to the barrel cortex, whereas the EYFP pattern was essentially uniform in the surrounding regions of cortex (Figure 1B; Figure S1C). The barrel-like units of EYFP were localized to the upper half of L6 (L6a) and were not evident in either lower L6 (L6b) or L5 (Figure 1B, right). The most clearly defined EYFP units were located above the fimbria and hippocampus, coincident with the location of the largest L4 barrels. Analysis of the spatial patterns of fluorescence intensity revealed that the EYFP in L6a correlated closely with the VGLuT2 in L4, indicating that the barrel-like units of EYFP were aligned with L4 barrels (Figure 1C). Because of their barrel-like appearance and infragranular location, we call these L6a structures “infrabarrels.”

Large L4 barrels in the posteromedial barrel subfield (PMBSF) are somatotopically arranged in the pattern of mystacial vibrissae on the snout, and barrel neurons respond rapidly to vibrissa deflections (Simons, 1978; Woolsey and Van der Loos, 1970). We examined the spatial distribution of infrabarrels in *Ntsr1:ChR2-EYFP* mice by preparing brain sections cut tangential to the cortical surface. Viewed this way, L6a infrabarrels were ellipsoidal and were distributed in distinct rows (Figure 1D, right). EYFP-expressing processes in L4, which include the dendrites, axons, and terminals of L6 CT cells, also formed similar rows of ellipsoids (Figure 1D, left). This distinct EYFP pattern was not evident in sections through L5 (Figure 1D, middle). The row-like pattern of L6a infrabarrels is consistent with the spatial organization of L4 barrels in the PMBSF, as observed with cytochrome oxidase staining (Figure 1E). These data strongly suggest that infrabarrels in the PMBSF are somatotopically arranged to mimic both the L4 barrels and the rows of vibrissae on the snout.

To distinguish axons from dendrites, we next crossed the synaptophysin (SYN)-tdTomato reporter line (Ai34d) with *Ntsr1-Cre* mice to express the red reporter selectively in the axonal processes of L6 CT neurons (Kim et al., 2014). Again, imaging live and fixed tissue revealed a periodic tdTomato pattern in L6a that was aligned with L4 barrels (Figures 2A and 2B). Thus, the intracortical axons of CT cells can delineate infrabarrels even without appreciable somatodendritic labeling. CT axonal processes were particularly dense in L5a, consistent with a previous study (Kim et al., 2014). We observed, unexpectedly, that CT axonal processes were also dense in the lower half of L4 septa, more so than within L4 barrels (Figures 2B and 2C). These data revealed that the intracortical processes of L6 CT axons have a distinct laminar and columnar organization, suggesting that L6 CT output may have important consequences for barrel- and septum-related circuit function at multiple levels within the cortical column.

In summary, L6a contains discrete cytoarchitectonic units—infrabarrels—that are clearly identifiable in live and fixed tissue, include the axonal processes of CT neurons, and are spatially aligned with the well-characterized barrels of L4.

CT Neurons and Infrabarrels

To understand the cellular organization of infrabarrels, we analyzed the spatial distribution of neurons across L6a in the

barrel cortex. Some studies of the rat barrel cortex have described a patchy, discontinuous distribution of CT neurons following injections of retrograde tracers in the thalamus, but only a fraction of CT cells are labeled with this approach (Chmielewska et al., 1989; Killackey and Sherman, 2003; Staiger et al., 1996; Wise and Jones, 1977). To examine the distribution of neurons across infrabarrels, we counted CT and non-CT neurons using tissue samples prepared from *Ntsr1:ChR2-EYFP* mice that were immunolabeled for both VGLuT2 and NeuN, a neuron-specific marker (Figure 3A). CT and non-CT neurons were identified by Cre-dependent expression of ChR2-EYFP in their membranes (Figure 3B). Cells that could not be definitively defined were excluded (~8% of NeuN-positive cells).

Using VGLuT2 imaging in L4 to normalize the location of each neuron (see the Experimental Procedures), we found that the density of CT neurons in L6a was higher within a barrel column than in the septa between infrabarrels: CT cell density in L6a was positively correlated with VGLuT2 fluorescence in L4 (Figure 3C). In contrast to CT neurons, the density of non-CT cells in L6a was higher in septa and negatively correlated with VGLuT2 fluorescence in L4 (Figure 3D). The entire sample of NeuN-positive cells in L6a was evenly distributed (Figure 3E). We found that CT cells also make up the majority of neurons in L6a, consistent with previous reports (Kim et al., 2014; Olsen et al., 2012; Zhang and Deschênes, 1997) (CT = $56.3\% \pm 0.9\%$, non-CT = $43.7\% \pm 0.9\%$; mean \pm SEM; $n = 8$ barrel columns, 4 hemispheres, and 3 mice). Thus, in the mouse barrel cortex there is an inverse relationship between the densities of CT and non-CT cells in L6a as they relate to barrel columns and septa (Figure 3F).

Which neurons account for the distribution of non-CT cells in L6a? Non-CT neurons in L6 comprise two broad populations: (1) excitatory CC projection neurons, which account for all other excitatory cells within this layer; and (2) inhibitory interneurons, which comprise about 10% of all neurons in L6 (Olsen et al., 2012; Zhang and Deschênes, 1997). To investigate this further, we analyzed the distribution of inhibitory interneurons in L6a of *Ntsr1:ChR2-EYFP* mice using a strategy similar to that described above. We immunolabeled parvalbumin (PV)- and somatostatin (SOM)-expressing cells, the two predominant types of interneurons in infragranular layers (Tremblay et al., 2016). Analysis of the horizontal distribution of PV- and SOM-expressing cells revealed no correlation with infrabarrels (Figure S2), indicating that inhibitory interneurons are not responsible for the differential distribution of non-CT cells.

In summary, our results show that somata of excitatory CT neurons in L6a tend to be clustered within barrel columns while excitatory CC projection neurons preferentially occupy septa in L6a. Inhibitory interneurons are evenly distributed. We conclude that the infrabarrels embody a unique spatial organization of excitatory projection cells, most notably the L6 CT neurons.

Physiological Properties of L6a Neurons

We identified a differential clustering of two excitatory projection neurons in L6a, each with different downstream targets. Previous studies showed that L6 CT and CC neurons exhibit distinctive intrinsic properties, including excitability (Brumberg et al., 2003; Kinnischtzke et al., 2016; Kumar and Ohana, 2008; Vélez-Fort et al., 2014; Yang et al., 2014); however, the results

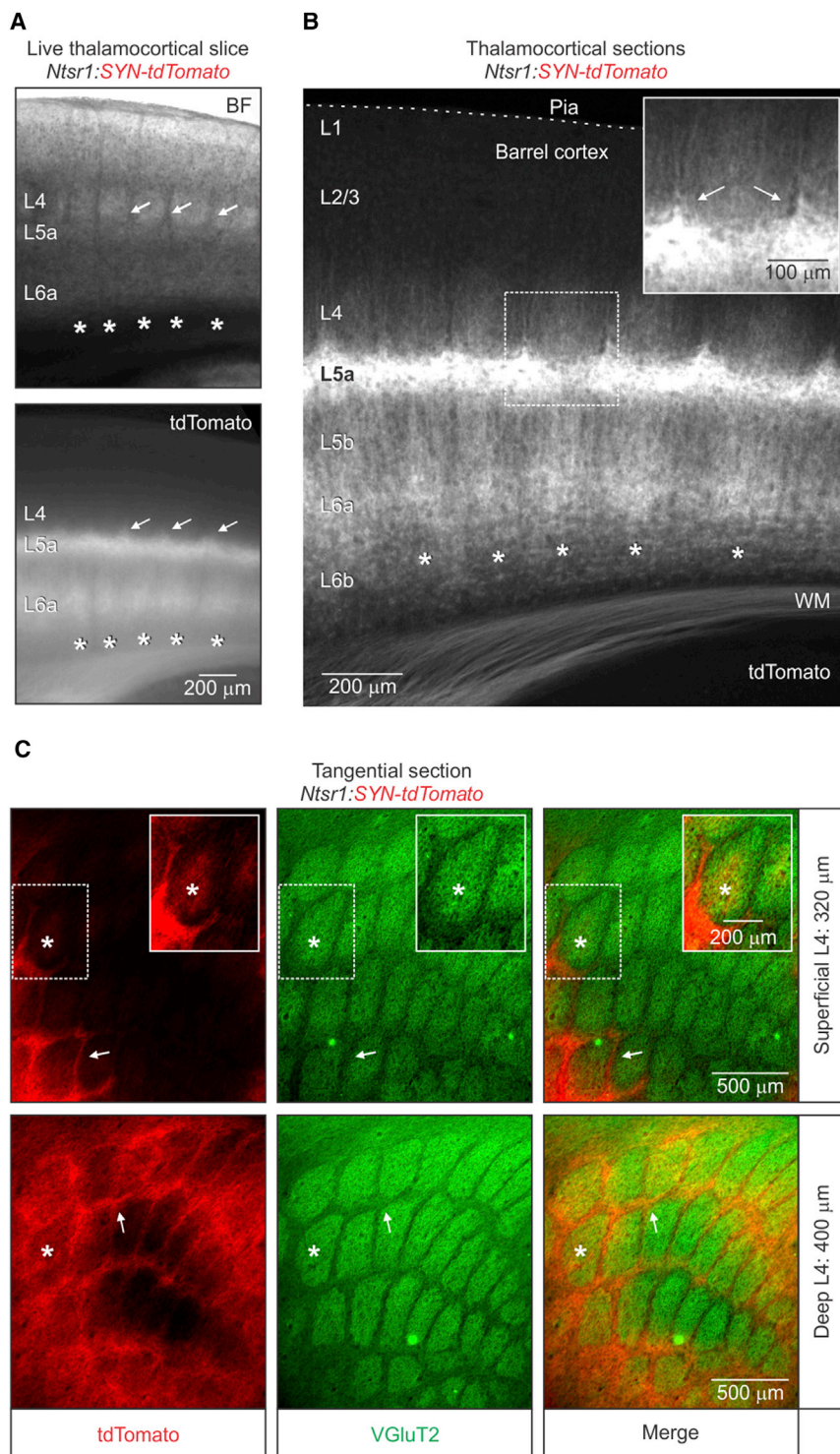


Figure 2. Organization of L6 CT Axon Collaterals in the Barrel Cortex

(A) (Top) Bright-field (BF) image and epifluorescence image (bottom) showing the expression pattern of tdTomato in a live 300- μ m-thick thalamocortical slice through the barrel cortex of a 34-day-old *Ntsr1:synaptophysin(SYN)-tdTomato* mouse. In addition to the periodic pattern of tdTomato in L6a (asterisks), there was a robust expression in both L5a and L4 septa (arrows). (B) Image of an 80- μ m-thick brain section, taken from the live slice shown in (A). The inset shows tdTomato in L4 septa (arrows). Similar patterns were observed in 4 hemispheres from 2 mice. (C) Fluorescent images of adjacent 80- μ m-thick tangential sections through the L4 barrel cortex of a 56-day-old *Ntsr1:SYN-tdTomato* mouse. The expression of tdTomato in L4 was particularly robust in the septa (arrows) between barrels stained immunohistochemically for VGlut2. The inset image shows the presence of tdTomato in the barrel center after additional contrast enhancement. The asterisk denotes the approximate location of an individual barrel in adjacent sections. A similar pattern of tdTomato was seen in repeated experiments ($n = 4$ hemispheres from 2 mice).

cells in *Ntsr1-Cre* mice crossed to a tdTomato reporter (*Ai9* or *Ai14*) (Figure 4; Figure S3). We also examined the properties of genetically defined and retrogradely labeled non-CT cells in L6 (that is, *PV-Cre*, *SOM-Cre*, *5HT3aR-GFP*, and CC projection neurons) (Figures S4 and S5). We found that the vast majority of tdTomato-negative cells in L6a had regular-spiking physiological properties and that this phenotype was a distinguishing feature of CC cells in L6a of the mouse barrel cortex (Figures S3 and S5). L6a regular spiking cells were also physiologically distinct from PV-, SOM-, and 5HT3aR-expressing interneurons located in L6 (Figure S4; Table S1). A few cells could not be definitively assigned to a group and were, therefore, excluded ($n = 8$ neurons from 27 mice; Figure S3).

Intrinsic membrane properties also distinguished L6a CC neurons (that is, tdTomato negative with regular spiking physiology) from CT neurons (that is, tdTomato positive) (Figure 4; Table S2). Specifically, the input resistance of CT cells was larger, input capacitance was

smaller, and membrane time constant was briefer when compared to CC cells (Figure 4C). The two types of neurons had similar resting membrane potentials (~ -84 mV). Despite their larger resting input resistance, the rheobase of CT cells was nearly twice that of CC cells (Figure 4D). This difference

of these studies differed substantially. Clarifying these differences is critical for understanding L6 circuit mechanisms. To facilitate an electrophysiological study of L6a, we first systematically examined the intrinsic membrane properties of CT and non-CT neurons by recording tdTomato-positive and -negative

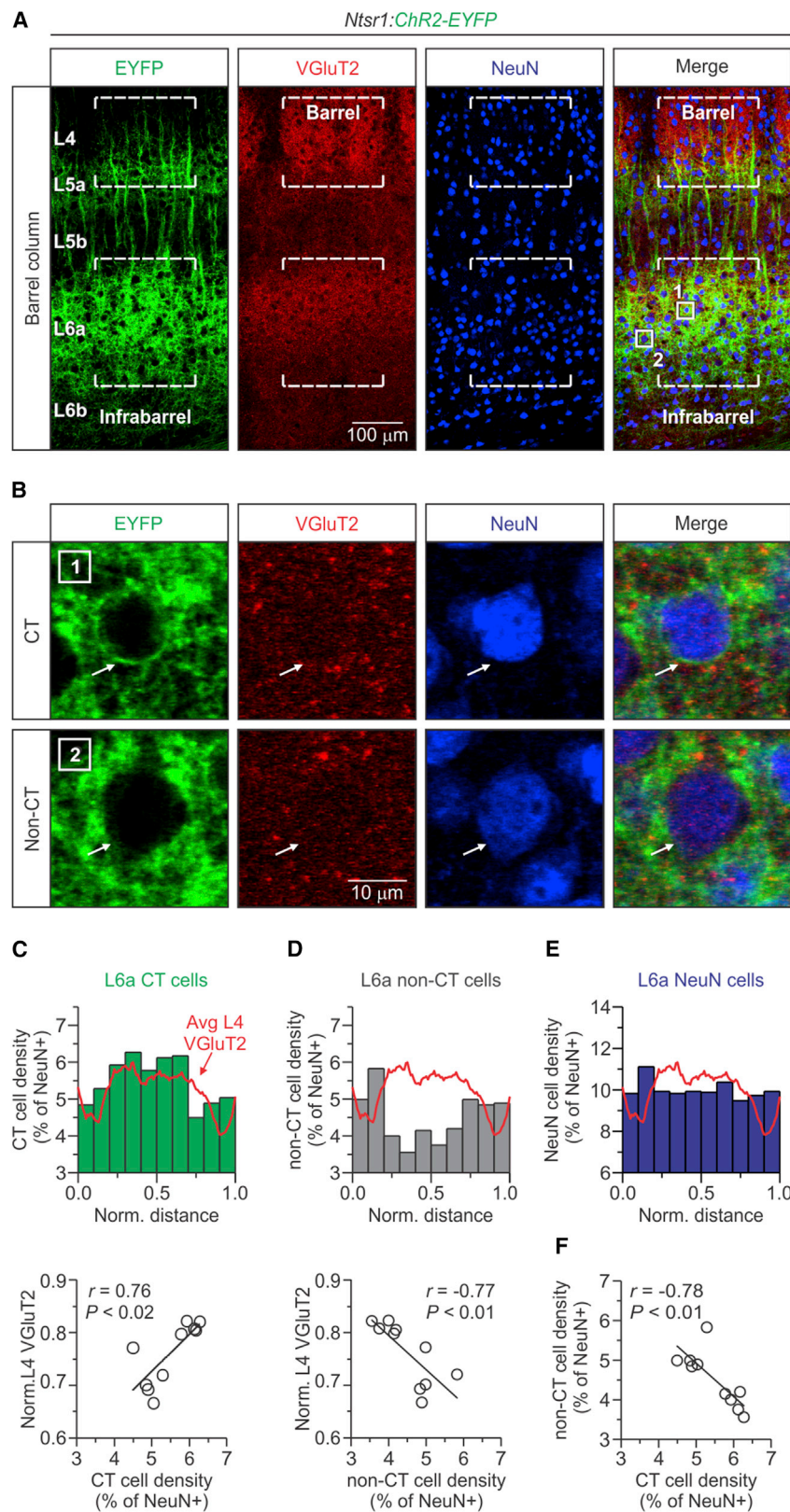


Figure 3. The Cytoarchitecture of L6a Infrabarrels

(A) Confocal images of an aligned L4 barrel and L6a infrabarrel (dashed lines) taken from a 25-day-old *Ntsr1:ChR2-EYFP* mouse. The example shown is the number 3 barrel column in Figure 1B. Tissue was stained immunohistochemically for VGluT2 and NeuN.

(B) High-magnification image of the boxed areas in (A, far right) showing two types of NeuN-positive cells. CT and non-CT neurons were identified by the Cre-dependent expression of ChR2-EYFP in their membranes (arrow).

(C) (Top) A normalized distribution plot of L6a CT cells ($n = 1,110$ CT cells, 8 barrel columns, 4 hemispheres, and 3 mice). The red trace represents the average fluorescence intensity of L4 VGluT2 for all columns examined. (Bottom) Plot shows a strong and significant positive correlation between the density of CT neurons per bin and L4 VGluT2 ($r = 0.76$, $p = 0.010$, Pearson's correlation coefficient).

(D) (Top) Normalized distribution of L6a non-CT cells ($n = 915$ non-CT cells, 8 barrel columns, 4 hemispheres, and 3 mice). (Bottom) Plot shows a strong and significant negative correlation between the density of non-CT neurons per bin and L4 VGluT2 ($r = -0.76$, $p = 0.009$, Pearson's correlation coefficient).

(E) A normalized distribution plot of all L6a NeuN cells. There was no correlation between the density of all L6a neurons and L4 VGluT2 (data not shown; $r = 0.79$, $p = -0.093$, Pearson's correlation coefficient).

(F) Plot showing a strong and significant negative correlation between the density of L6a non-CT and CT neurons per bin ($r = 0.76$, $p = 0.010$, Pearson's correlation coefficient).

See also Figure S2.

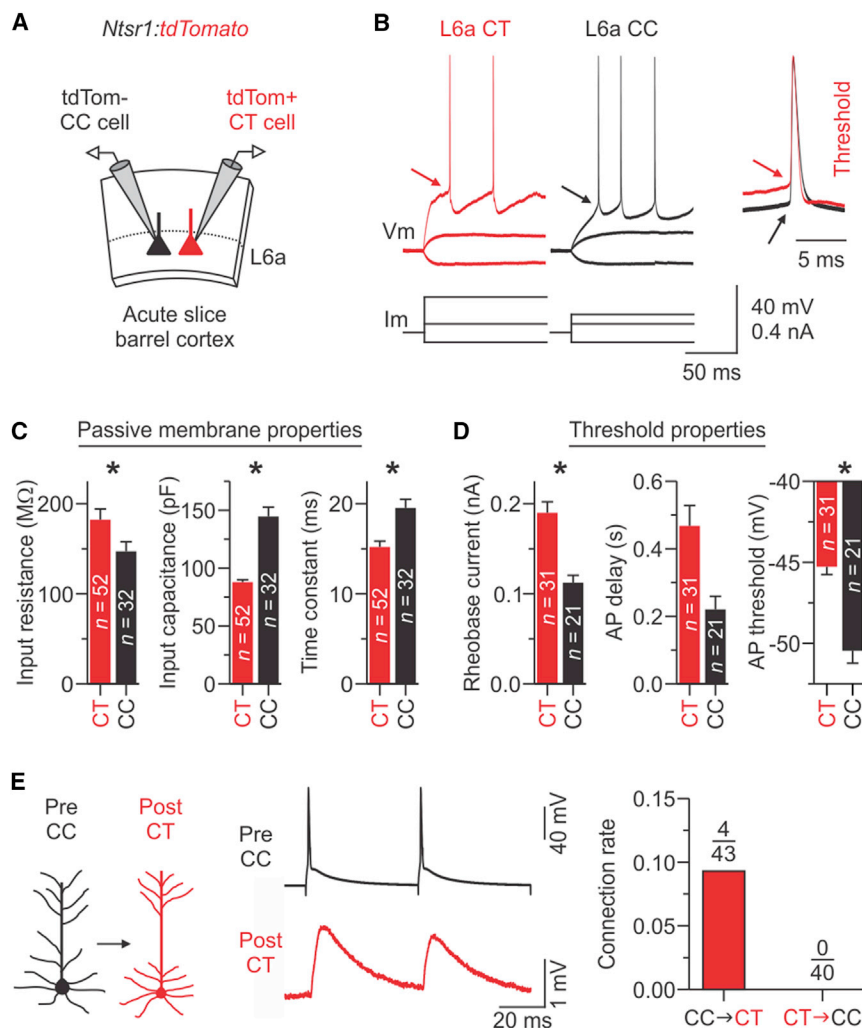


Figure 4. Intrinsic Physiological Properties of CT and CC Cells in L6a

(A) Schematic of the slice recording configuration. L6a CT cells were identified by Cre-dependent tdTomato expression, while CC cells were identified as tdTomato negative and physiologically as regular spiking (see Figures S3–S5).

(B) Voltage responses to injected current of representative CT and CC cells. Evoked action potentials (APs) required more current to reach threshold (arrow, inset) in CT cells than in CC cells. (C and D) Histograms showing the mean \pm SEM for key passive properties (C) and AP threshold properties (D). Asterisks indicate statistical significance. See Table S1 for summary statistics for all intrinsic properties.

(E) (Left and middle) Unitary EPSPs in a CT cell evoked by APs in a CC (trace represents the average of 15 trials, train of two APs at 20 Hz; holding potentials for both cells were -84 mV). (Right) Summary graph of the connection rate between CT and CC neurons is shown. In total, we found 0 CT-to-CC connections (0.0%; $n = 40$ pairs tested in 23 mice) and 4 CC-to-CT connections (9.3%; $n = 43$ pairs tested in 24 mice) with mean unitary EPSP amplitudes of 0.7 ± 0.2 mV on the first AP (see Figure S8).

Summary statistics are as follows: input resistance: CT cells = 182.2 ± 12.0 M Ω ; CC cells = 147.1 ± 10.7 M Ω ; $n = 52/32$ CT/CC cells from 24/20 mice; $p = 0.0348$, two-tailed Mann-Whitney U test; input capacitance: CT cells = 87.9 ± 2.1 pF; CC cells = 144.6 ± 8.0 pF; $n = 52/32$ cells from 24/20 mice; $p = 6.44 \times 10^{-11}$, two-tailed Mann-Whitney U test; time constant: CT cells = 15.2 ± 0.7 ms; CC cells = 19.5 ± 1.0 ms; $n = 52/32$ cells from 24/20 mice; $p = 5.22 \times 10^{-5}$, two-tailed Mann-Whitney U test; rheobase current: CT cells = 190.0 ± 12.2 pA; CC cells = 112.4 ± 8.2 pA; $n = 31/21$ cells from 16/12 mice; $p = 1.64 \times 10^{-5}$, two-tailed t test; AP delay: CT cells = 468.0 ± 60.0 ms; CC cells = 220.6 ± 38.7 ms; $n = 31/21$

cells from 16/12 mice; $p = 0.05187$, two-tailed Mann-Whitney U test; and AP threshold: CT cells = -45.3 ± 0.5 mV; CC cells = -50.5 ± 0.8 mV; $n = 31/21$ cells from 16/12 mice; $p = 2.18 \times 10^{-7}$, two-tailed t test. Data are represented as mean \pm SEM. See also Figures S3–S5 and S8 and Tables S1 and S2.

was due, at least partly, to a 5 mV higher spike threshold and a larger voltage difference between rest and threshold in CT cells, as compared to CC cells (Figure 4D). Similarly, we found that the delay to spike onset at rheobase for CT cells was more than double that of CC cells, although not statistically significant ($p = 0.052$; Figure 4D). Lastly, the two cell types had several differences in the properties of individual action potentials and spike frequency adaptation during moderate spike rates (Table S2).

Together, these results demonstrate that L6a CT and CC neurons have distinctive intrinsic physiological properties. These data also revealed that L6a CT cells are intrinsically less excitable than CC cells.

Thalamocortical Inputs to Infrabarrel Projection Neurons

The thalamus is the main source of extrinsic input to the neocortex. As a result, the ascending thalamocortical pathways have been extensively studied (Cruikshank et al., 2007, 2010; Gabernet et al., 2005; Oberlaender et al., 2012; Petreanu et al.,

2009). The barrel cortex receives two main types of somatosensory inputs that originate from different thalamic nuclei: the ventral posterior medial nucleus (VPM) and the posterior medial nucleus (POM) (Chmielowska et al., 1989; Wimmer et al., 2010). While many studies have examined the impact of these pathways on the barrel cortex, they overlooked L6, failed to identify the postsynaptic cell types in L6, or used non-specific electrical stimulation to activate thalamic axons (Audette et al., 2017; Beierlein and Connors, 2002; Bureau et al., 2006; Cruikshank et al., 2010; Petreanu et al., 2009; Yang et al., 2014). To investigate pathway-specific responses in distinct classes of L6 excitatory cells, we combined optogenetic control strategies with cell-type-specific genetics and whole-cell recordings using an acute *in vitro* preparation (Agmon and Connors, 1991; Crandall et al., 2015; Cruikshank et al., 2010).

We first targeted ascending VPM axons for optogenetic manipulation by injecting an adeno-associated virus (AAV, serotype 2/2) expressing ChR2-EYFP into the VPM of *Ntsr1:tdTomato* mice (Figure 5A, left). After 10–15 days, we

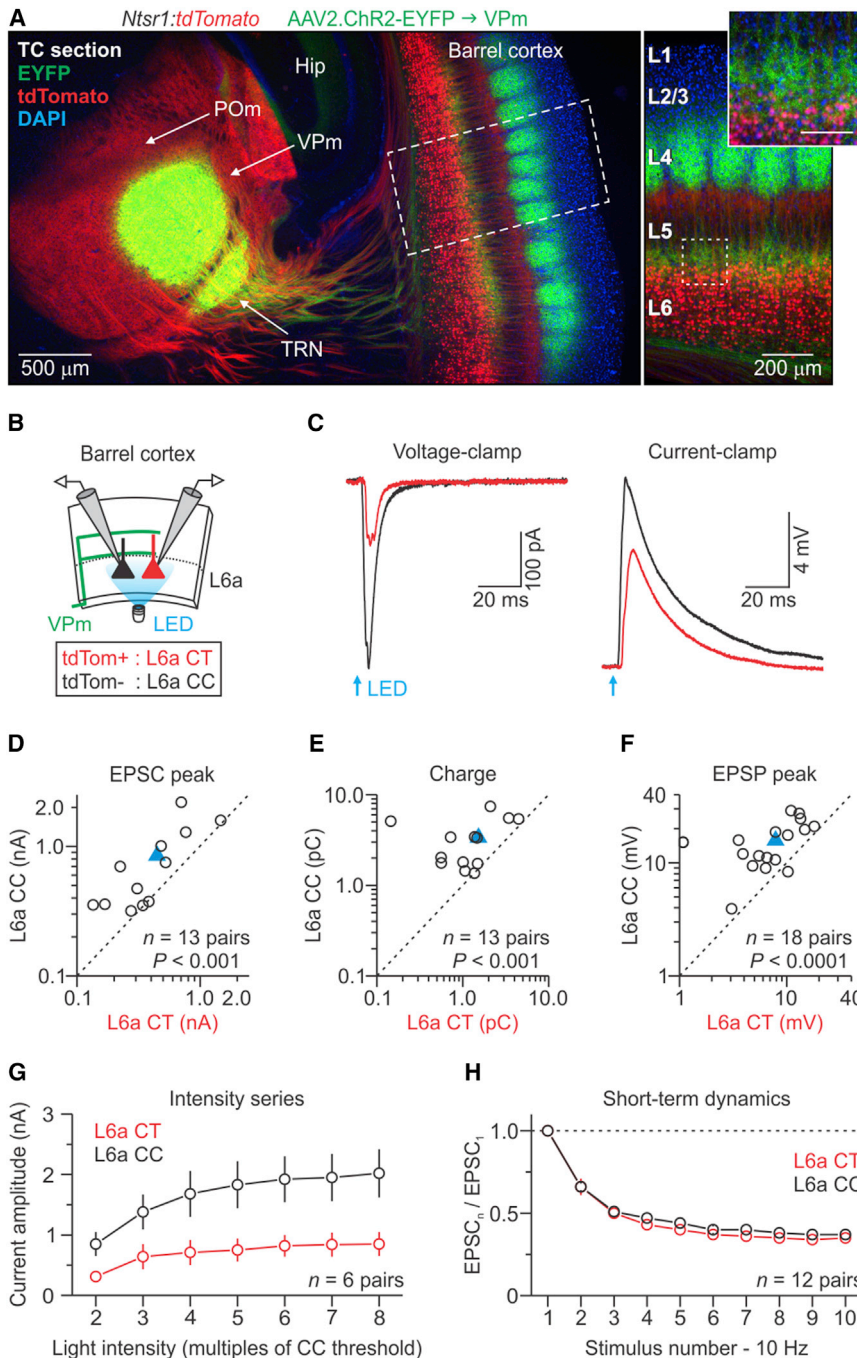


Figure 5. VPM-Evoked Synaptic Responses in Pyramidal Neurons of L6a

(A) (Left) Low-magnification fluorescence image taken of a fixed thalamocortical (TC) section (40 μ m thick) showing EYFP expression 13 days after injecting a virus (AAV2) carrying genes for ChR2-EYFP into the VPm of a *Ntsr1:tdTomato* mouse. The section was counterstained with DAPI. (Right) High-magnification image shows EYFP-labeled VPm axons terminating densely in L4 barrels and at the L5/6 border (inset: scale bar, 100 μ m).

(B) Schematic of the recording configuration showing photostimulation of ChR2-expressing VPm axons (green) and recordings from CT-CC cell pairs.

(C) EPSCs and EPSPs for a CT and CC cell pair in response to activation of VPm axons (voltage clamp at -94 mV and current clamp at -84 mV; 1-ms-light pulse duration; traces represent the average of 15 voltage-clamp and 7 current-clamp trials). Light intensities were $\sim 3\times$ threshold for evoking an EPSP in CC cells (mean intensity = 0.90 ± 0.17 mW; $n = 18$ pairs from 9 mice).

(D–F) Summary data plots for EPSC peak (D), charge (E), and EPSP peak (F). Blue triangles represent means.

(G) VPm-evoked EPSCs were larger in CC than CT cells over a range of light intensities ($n = 6$ pairs from 4 mice).

(H) Short-term dynamics of ChR2-evoked VPm responses (EPSC peak) across 10-Hz trains were similar for CC and CT cells ($n = 12$ pairs from 7 mice).

Summary statistics are as follows: EPSP threshold intensity (data not shown): CT = 0.44 ± 0.09 mW; CC cells = 0.32 ± 0.06 mW; $n = 17$ pairs from 9 mice, one pair was not included because the CT cell did not respond; $p = 4.88 \times 10^{-4}$, two-tailed paired Wilcoxon signed-rank test; EPSC peak (D): CT cells = 448.3 ± 103.5 pA; CC cells = 848.8 ± 163.4 pA; $n = 13$ pairs from 7 mice; $p = 7.32 \times 10^{-4}$, two-tailed paired Wilcoxon signed-rank test; EPSC charge (E): CT cells = 1.52 ± 0.34 pC; CC cells = 3.36 ± 0.54 pC; $n = 13$ pairs from 7 mice; $p = 4.88 \times 10^{-4}$, two-tailed paired Wilcoxon signed-rank test; and EPSP peak (F): CT cells = 7.9 ± 1.2 mV; CC cells = 15.8 ± 1.6 mV; $n = 18$ pairs from 9 mice; $p = 3.40 \times 10^{-5}$, two-tailed paired t test. Data are represented as mean \pm SEM. See also Figure S6.

observed EYFP-expressing VPm axons and terminals concentrated in L4 barrels and, to a lesser extent, at the L5b/L6a border (Figure 5A, right), consistent with the known projection pattern of VPm neurons (Cruikshank et al., 2010; Wimmer et al., 2010). When VPm cells in the injection site were directly photostimulated in the presence of fast synaptic blockers, they depolarized with very short onset latencies (<0.6 ms), confirming they were expressing ChR2 (Figures S6A–S6D) (Cruikshank et al., 2010).

To investigate VPm inputs to L6a, we photostimulated VPm axon terminals in the cortex while recording from mixed pairs of neurons (Figure 5B). This strategy controlled for variability in ChR2 expression levels across slices and mice. Each cell pair consisted of one tdTomato-positive CT and one tdTomato-negative CC neuron in L6a, the latter further identified by its regular spiking physiology. To isolate VPm responses, we recorded in voltage and current clamp using a potassium-based internal solution to measure both excitatory postsynaptic currents (EPSCs) and potentials (EPSPs) evoked by brief (1-ms) wide-field illumination. When VPm axons were photostimulated,

EPSCs recorded in voltage clamp were usually larger in CC cells than in CT cells (Figures 5C–5E). Onset latencies were significantly faster for CC than CT cells (CC cells = 2.08 ± 0.07 ms; CT cells = 2.43 ± 0.12 ms; $n = 13$ pairs from 7 mice; $p = 0.0118$, two-tailed paired *t* test). Similarly, EPSPs recorded in current clamp were consistently larger in CC than in CT cells (Figures 5C and 5F). VPM-triggered EPSCs and EPSPs were about twice as strong in CC cells as in CT cells. Importantly, VPM-EPSCs were larger in CC cells across a range of photostimulation intensities (Figure 5G). When VPM inputs were activated at 10 Hz, EPSCs in both postsynaptic cell types displayed strong short-term depression (Figure 5H).

To rule out the possibility that retrograde viral expression of ChR2 contributed to the excitation of L6 neurons, we further examined the light-evoked responses. The latencies to response in all cells were ~ 2 ms, which is significantly longer than the direct ChR2-mediated current latencies recorded in VPM cells themselves (Figure S6D). Furthermore, the responses of the L6 cells were blocked by AMPA- and NMDA-type glutamate receptor antagonists (DNQX, 20 μ M; and APV [DL-2-amino-5-phosphonopentanoic acid], 50 μ M) (Figures S6E–S6H). Thus, L6 cells did not undergo retrograde viral infection, and light-evoked VPM responses were synaptic in nature, mediated by ionotropic glutamate receptors.

Next, we investigated POM-evoked synaptic responses in L6 projection neurons using the same optogenetic strategy and virus. Injections into POM produced strong ChR2-EYFP expression in POM axons within the barrel cortex (Figure 6A). Dense expression was observed in L5a, L4 septa, and L1, consistent with the known projection pattern of POM neurons (Wimmer et al., 2010). Photoactivation of POM fibers in the cortex evoked much larger EPSCs and EPSPs in L6a CC cells than in CT cells (Figures 6C–6F). The synaptic latencies in CC cells were about half those of CT cells (CC cells = 2.54 ± 0.19 ms; CT cells = 4.85 ± 0.82 ms; $n = 8$ pairs from 5 mice; $p = 0.0330$, two-tailed paired *t* test). In 14 pairs of CT–CC cells tested, we recorded reliable synaptic responses from all CC neurons (100%). By contrast, only 8 of the CT cells (57%) generated responses, and all of those were small and slow. Notably, CT neurons responded poorly to POM inputs even at higher light intensities (Figure 6G). Finally, POM-evoked EPSCs underwent strong short-term depression at 10 Hz, similar to the responses obtained from repetitive activation of VPM axons (Figure 6H).

Interestingly, we frequently observed that single, brief, wide-field photostimulation of POM axons (but not VPM axons) resulted in persistent barrages of excitatory input in CC cells following the initial monosynaptic response (Figure S7). This persistent activity was likely mediated by other local excitatory neurons, yet it was never observed in simultaneously recorded CT cells. The specificity of this activity for CC, but not CT, cells implies even further segregation of CC and CT circuits within L6.

These results clearly indicate that L6a CC and CT cells receive different signals from the two thalamocortical pathways, so we next asked how these signals are communicated intracortically using paired whole-cell recordings to determine the synaptic connectivity between L6a CC and CT cells. Overall, we found that L6a excitatory neurons formed sparse, selective, non-recip-

rocal excitatory synapses onto each other: L6a CC cells formed synapses onto CT cells in 9.3% of tested pairs, whereas CT cells never excited CC cells (Figure 4E). Although our paired recordings did not reveal any CT-to-CC connections, broad photostimulation of ChR2-expressing CT cells evoked weak EPSPs in CC cells, implying a low probability of CT-to-CC synapses (Figure S8).

Together, these results suggest that L6a CC and CT cells form two partially segregated excitatory circuits that control the flow of information to and from the cortex, linking specific thalamocortical inputs with distinct outputs.

DISCUSSION

We found that L6a contains a well-defined array of barrel-shaped modules, infrabarrels, that are topographically aligned with L4 barrels (Figure 7). Our analysis revealed that CT neurons and their local axon collaterals are densest within infrabarrels, whereas CC neurons are more prevalent in the septa between infrabarrels. The clustering of CT axons within infrabarrels is likely to reflect the clustering of CT somata and the sparseness of their local axons (Narayanan et al., 2015). Inhibitory interneurons do not respect infrabarrel boundaries.

Combining optogenetics with paired whole-cell recordings, we found that CC cells receive strong synaptic inputs from both VPM and POM thalamic nuclei, whereas CT cells respond more weakly to VPM input and are largely untouched by POM. During trains of stimulation, both the excitatory VPM and POM responses in L6 underwent similar short-term depression, a frequently described feature of thalamocortical synapses (Beierlein and Connors, 2002; Cruikshank et al., 2010; Gabernet et al., 2005; Yang et al., 2014). Moreover, we found that local synaptic connections between CT and CC neurons are relatively sparse and not reciprocal, consistent with previous work in the sensory cortex of different species (Beierlein and Connors, 2002; Lefort et al., 2009; Mercer et al., 2005). Together, these results reveal the structural and functional organization of two partially segregated excitatory circuits in L6a that directly link thalamocortical inputs with distinct outputs to the thalamus and other areas of the cortex.

In sensory cortices, anatomical and physiological data emphasize a core columnar circuit composed of an ensemble of vertical connections that serve to transform excitation along the L4 \rightarrow L2/3 \rightarrow L5/6 pathway (Douglas and Martin, 2004). L4 is the primary recipient layer of specific thalamic afferents, yet collaterals of these same axons also innervate L5/6 (Beierlein and Connors, 2002; Chmielowska et al., 1989; Constantinople and Bruno, 2013; Cruikshank et al., 2010; Oberlaender et al., 2012; Wimmer et al., 2010; Yang et al., 2014), suggesting a role for infragranular layers in early thalamocortical processing. Recently, Constantinople and Bruno (2013) demonstrated that sensory responses in L5/6 of the rat barrel cortex might not require L4, implying that the thalamus activates upper and lower layers in parallel. Our results add to mounting evidence that infragranular layers are important sites of early thalamocortical processing within the neocortex, and they begin to define how L6 excitatory circuits integrate thalamic signals during sensory processing.

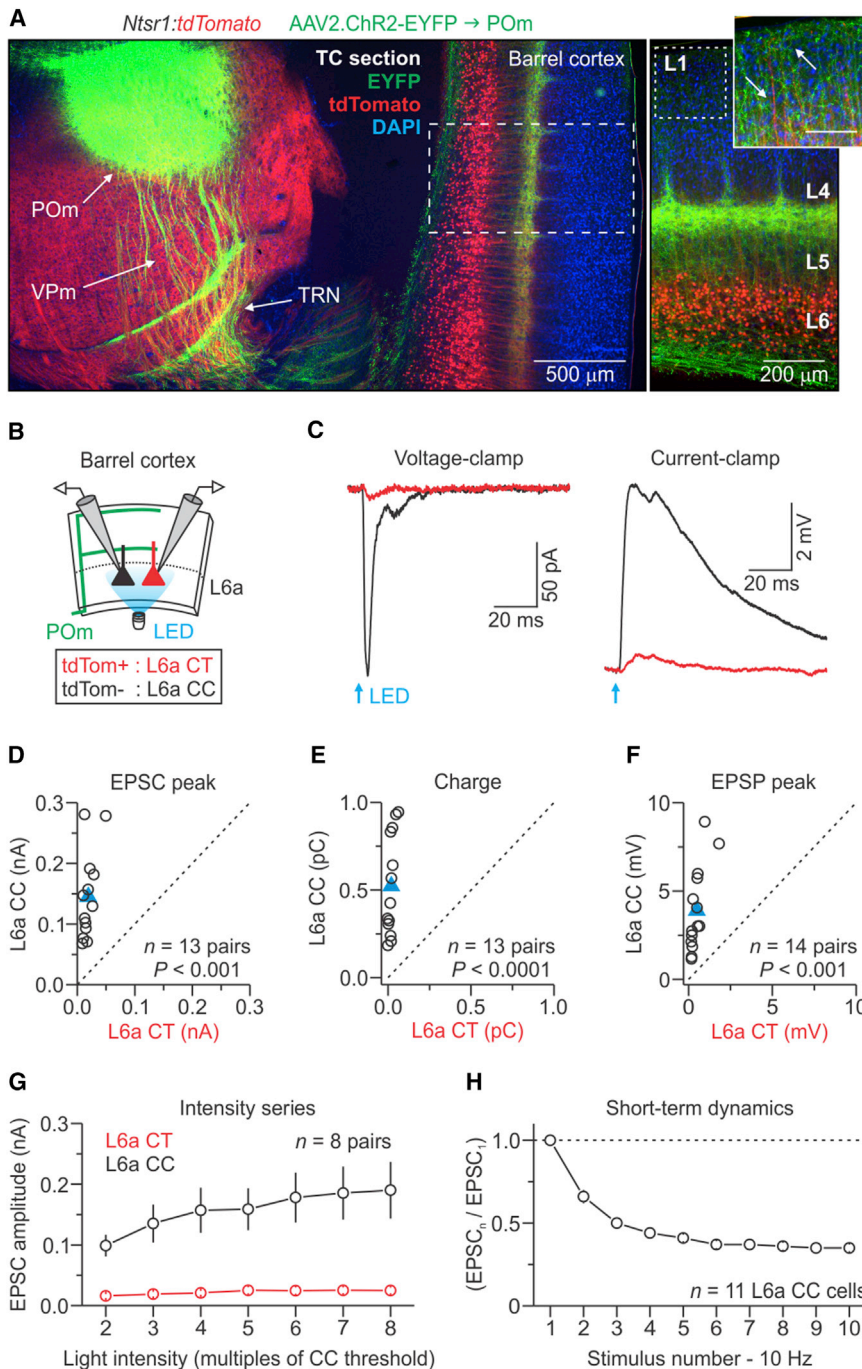


Figure 6. POM-Evoked Synaptic Responses in Pyramidal Neurons of L6a

(A) (Left) Low-magnification fluorescence image taken of a fixed thalamocortical (TC) section (40 μ m) showing EYFP expression 11 days after injecting a virus (AAV2) carrying genes for ChR2-EYFP into the POm of a *Ntsr1:tdTomato* mouse. The section was counterstained with DAPI. (Right) High-magnification image shows EYFP-labeled POm axons in L5a, L4 septa, and L1 (inset: scale bar, 100 μ m). Arrows in inset point to both POm (green) and L6 CT (red) processes in L1.

(B) Schematic of the recording configuration.

(C) EPSCs and EPSPs for an L6a CT and CC cell pair in response to activation of POm axons (voltage clamp at -94 mV and current clamp at -84 mV; 1-ms pulse duration; traces represent the average of 16 voltage-clamp and 9 current-clamp trials). Light intensities were $\sim 3\times$ threshold for evoking an EPSP in CC cells (mean power = 4.9 ± 1.0 mW, $n = 14$ pairs from 7 mice).

(D–F) Summary data plots for EPSC peak (D), charge (E), and EPSP peak (F). Blue triangles represent means.

(G) POM-evoked EPSCs were much larger in CC than CT cells over a range of light intensities ($n = 8$ pairs from 5 mice).

(H) Short-term dynamics of POM-evoked responses (EPSCs) across 10-Hz trains for CC cells ($n = 11$ neurons from 5 mice).

Summary statistics are as follows: EPSC peak (D): CT cells = 19.1 ± 3.1 pA; CC cells = 145.0 ± 19.9 pA; $n = 13$ pairs from 7 mice; $p = 2.44 \times 10^{-4}$, two-tailed paired Wilcoxon signed-rank test; EPSC charge (E): CT cells = 0.02 ± 0.01 pC; CC cells = 0.52 ± 0.08 pC; $n = 13$ pairs from 7 mice; $p = 2.35 \times 10^{-5}$, two-tailed paired t test; and EPSP peak (F): CT cells = 0.5 ± 0.1 mV; CC cells = 3.9 ± 0.6 mV; $n = 14$ pairs from 7 mice; $p = 1.22 \times 10^{-4}$, two-tailed paired Wilcoxon signed-rank test. Data are represented as mean \pm SEM. See also Figures S7 and S8.

and project to septa in S1 (Bokor et al., 2008; Furuta et al., 2009; Pierret et al., 2000; Yu et al., 2006). Our approach cannot distinguish the relative contributions of these pathways to the responses of L6a cells. It would be interesting, however, to know whether the differences in CT and CC responses reflect properties of different afferent

pathways, a convergence of inputs from within or across pathways, or synapse distributions along each neuron's somatodendritic axis.

Excitatory afferents from POm to L6a were even more selective than those from VPm. POm is a higher-order nucleus that is reciprocally connected with multiple cortical areas, including S1, and it is involved in the transfer of sensory and perhaps other types of information (Diamond et al., 2008; Groh et al., 2014; Sherman, 2016; Yamawaki and Shepherd, 2015). The functions

What types of thalamocortical signals are processed in L6a? Our results suggest that L6a receives direct excitatory input from VPm, with CC cells responding more strongly than CT cells. In rodents, the ascending lemniscal pathway passes through VPm, carrying primarily single-vibrissa signals to L4 barrels and the L5/6 border of S1 (Diamond et al., 1992, 2008; Feldmeyer et al., 2013). Two additional pathways also relay in VPm and project to S1. Unlike the lemniscal pathway, these pathways are thought to convey different information

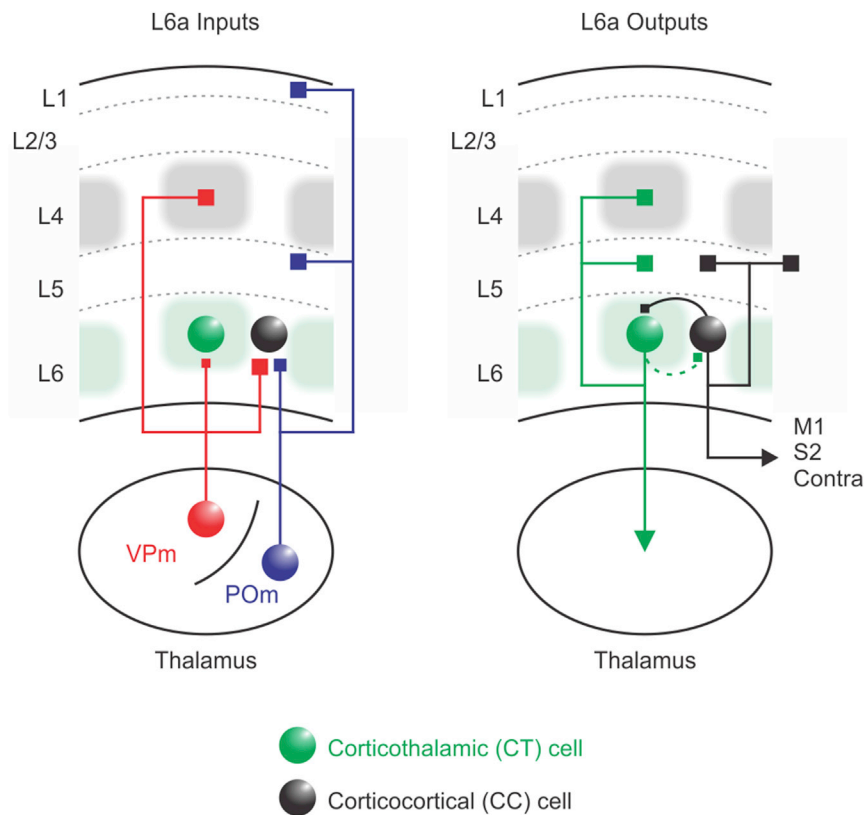


Figure 7. Schematic Illustration of the Excitatory Circuitry in L6a Infrabarrels and Surrounding Septa

(Left, input) CT cells in upper L6 are densest in the infrabarrels (green shadows), which are aligned with L4 barrels (gray). In contrast, CC projection cells are more prevalent in the surrounding septa. CC cells receive strong excitatory input from both VPm and POm thalamic nuclei, whereas CT cells receive weaker thalamocortical input, exclusively from the VPm. (Right, output) Previous work has shown that CT neurons in upper L6 project their axons to the thalamus and vertically within their home cortical column, whereas CC neurons have horizontally projecting axons that target infragranular layers of neighboring cortical columns and other cortical areas (Zhang and Deschênes, 1997). These two distinct excitatory circuits are also partially segregated from each other; local synaptic connections between CT and CC neurons are generally sparse and unidirectional, and they are most likely to go from CC cells to CT cells.

of POm are not entirely clear, but in rodents the paleomniscal pathway passes through POm and conveys complex multi-vibrissa signals (Ahissar et al., 2000; Diamond et al., 1992, 2008; Yu et al., 2006). Consistent with this possibility, recordings in the visual cortex of anesthetized mice showed that subthreshold receptive field properties of L6 CC cells had very broad stimulus selectivity, whereas L6 CT cells were much more narrowly tuned (Vélez-Fort et al., 2014). Since POm may also participate in cortico-thalamocortical communication (Sherman, 2016), POm afferents could transmit both ascending sensory and top-down CT signals to L6a (Groh et al., 2014). L6a CC cells are, therefore, in a unique position to integrate information from at least two parallel thalamocortical pathways.

CT cells are often reported to have low spontaneous rates and weak sensory responses *in vivo* (Oberlaender et al., 2012; Swadlow, 1989). We found that CT cells of mouse L6a are less intrinsically excitable than CC cells due to their higher spike threshold and rheobase, similar to CT cells in the rat barrel cortex (Kumar and Ohana, 2008). We suggest that both intrinsic membrane properties and weak thalamocortical inputs from the sensory thalamus contribute to the lack of sensory-evoked spiking activity of CT cells *in vivo*.

Although we did not distinguish subtypes of CT and CC cells in our study, previous work implies that the morphology of L6 projection cells are unusually diverse. For example, in the rodent barrel cortex, the VPm-projecting CT cells are found primarily in the upper half of the layer, whereas those projecting to POm and other thalamic nuclei are mostly located in L6b

cortical column (Zhang and Deschênes, 1997). In contrast, little is known about the organization of L6 CC cells. The axons of these cells are heterogeneous, targeting the infragranular layers of numerous cortical areas, including S1, S2, the motor cortex, and the contralateral cortex (Zhang and Deschênes, 1997). Interestingly, some CC cells, including those that project to the motor cortex (Alloway et al., 2004), are predominantly found within septum-related columns (Alloway, 2008).

The prevailing view of the barrel cortex is that it contains no cytoarchitectonic counterparts of barrels outside of L4 (Feldmeyer et al., 2013; Woolsey and Van der Loos, 1970). One of our major findings is that L6a contains infrabarrels, an array of discrete neuronal structures that are in perfect alignment with the pattern of PMBSF L4 barrels above. Such striking organization is common in the vibrissa sensory system. Barrelettes in the brainstem and barreloids in the thalamus are clusters of neurons that also mimic the arrangement of facial vibrissae (Ma, 1991; Van Der Loos, 1976). Thus, the identification of infrabarrels further defines the pathways of vibrissa sensation as well as those of thalamo-CT interactions more generally. Given their unique position between thalamic barreloids and cortical L4 barrels, infrabarrels may also play a role in the development of thalamocortical termination patterns in the cortex or perhaps the refinement of sensory-carrying afferents in the thalamus (Agmon et al., 1993; Thompson et al., 2016).

Each L4 barrel in the mouse appears as an ellipsoid-shaped cell-dense ring that surrounds a less cell-dense hollow (Woolsey and Van der Loos, 1970). In contrast to L4 barrels,

the ellipsoid-shaped infrabarrels in the mouse are filled with a relatively high density of CT neurons that span the full thickness of L6a. The cytoarchitecture of infrabarrels thus more closely resembles L4 barrels in the PMBSF of rats, which appear as solid, cell-dense clusters (Welker and Woolsey, 1974).

Infrabarrels and the clustered nature of L6 neurons became apparent to us while using transgenic mice that express fluorescent proteins selectively in CT cells (Bortone et al., 2014; Kim et al., 2014). Several studies have used retrograde-labeling techniques to visualize L6 CT neurons in the rodent barrel cortex, but the descriptions of their distribution have varied. CT neurons have been described as having an even distribution (Jacobson and Trojanowski, 1975; Killackey and Sherman, 2003) as well as a patchy, discontinuous distribution with cells clustered beneath L4 barrels (Chmielowska et al., 1989; Staiger et al., 1996; Wise and Jones, 1977) and L4 septa (Killackey and Sherman, 2003; Staiger et al., 1996). These differences may be due to the variability and nonuniformity of CT cell numbers and types that are retrogradely filled by thalamic injections.

We conclude that the mouse barrel cortex includes distinct cytoarchitectonic units in L6, the infrabarrels, that define functionally distinct circuits at several levels of analysis. Because infrabarrels are visible in both live and fixed tissue, they contribute to the advantages of the barrel cortex as a model for studying the neuronal and synaptic organization, functions, plasticity, and development of neocortical circuits.

EXPERIMENTAL PROCEDURES

Animal Protocols

All procedures were carried out in accordance with the NIH Guidelines for the Care and Use of Laboratory Animals and were approved by the Brown University Institutional Animal Care and Use Committee. Animals were maintained on a 12:12-hr light-dark cycle and provided food and water *ad libitum*. Both male and female animals were used in this study. The ages of mice used are described in the sections below. Experimental animals <28 days old were group-housed with their parents and littermates, whereas animals 28 days and older were housed in cages of four mice or less (same sex littermates).

Mice

We used the following mouse lines in this study: *Ntsr1-Cre* (received from C.I. Moore, Brown University, generated by the GENSAT project, available at the Mutant Mouse Regional Resource Centers [MMRRC], 030648-UCD) (Gong et al., 2007), *PV-Cre* (Jackson ImmunoResearch Laboratories, 008069), *SOM-IRES-Cre* (Jackson ImmunoResearch Laboratories, 013044), *5HT-3a-GFP* (received from R. Metherate, University of California, Irvine, generated by the GENSAT project, available at the MMRRC, 000273-UNC), *Ai9* (Jackson ImmunoResearch Laboratories, 007905) (Madisen et al., 2010), *Ai14* (Jackson ImmunoResearch Laboratories, 007908) (Madisen et al., 2010), *Ai32* (Jackson ImmunoResearch Laboratories, 012569) (Madisen et al., 2012), and *Ai34d* (Jackson ImmunoResearch Laboratories, 012570). The *Ntsr1-Cre* and *5HT-3a-GFP* mouse lines had CrI:CD1 (ICR) genetic backgrounds (Charles River Laboratories). All animals, except for the *5HT-3a-GFP* mice, were bred by crossing homozygous *Cre* mice with homozygous reporter mice, resulting in experimental mice that were heterozygous for the indicated genes.

Stereotactic Injections

AAV serotype 2 carrying genes for ChR2-EYFP fusion proteins was acquired from the University of North Carolina Viral Vector Core (rAAV2/hSyn-hChR2 [H134R]-eYFP-WPREA). The virus was injected into the right thalamus of mice *in vivo*, as previously described (Crandall et al., 2015; Cruikshank et al.,

2010). Briefly, for all surgeries mice were anaesthetized with a Ketaset-Dexdormitor mixture diluted in sterile saline (Ketaset, 70 mg/kg; Dexdormitor, 0.25 mg/kg; intraperitoneally [i.p.]). Once deeply anesthetized, mice were placed into a stereotaxic apparatus, and a craniotomy was made over the VPM or POM. Virus was then pressure-ejected into the brain via a glass micropipette attached to a Picospritzer pressure system (typically, 0.1–0.2 μ L over 10–20 min; titer = 2.00×10^{12} or $\sim 3.80 \times 10^{12}$ vector genomes [vg]/mL). The pipette was left in place for ~ 10 min before being slowly withdrawn from the brain. After surgery, mice were given Antisedan (2.5 mg/kg) to reverse the effects of Dexdormitor, and they were allowed to recover on a heating pad for ~ 1 hr before being returned to their home cage.

For VPM experiments, virus was injected into *Ntsr1: Ai9* ($n = 3$) or *Ntsr1: Ai14* ($n = 9$) mice *in vivo* between postnatal day 11 and 18 (mean age = 14.5 ± 0.7 days, $n = 12$ mice). The average stereotaxic coordinates from bregma for VPM injections were 1.9 mm lateral, -0.8 mm posterior, and 3.0 mm depth. VPM experiments were performed on mice 10–15 days after virus injection to allow for sufficient ChR2 expression (mean expression time = 11.9 ± 0.5 days). For POM experiments, virus was injected into *Ntsr1: Ai9* ($n = 2$) or *Ntsr1: Ai14* ($n = 5$) mice *in vivo* between postnatal day 11 and 15 (mean age = 13.0 ± 0.7 days, $n = 7$ mice). The average stereotaxic coordinates from bregma for POM injections were 1.4 mm lateral, -1.1 mm posterior, and 2.8 mm depth. POM experiments were performed on mice 11–16 days after virus injection to allow for sufficient ChR2 expression (mean expression time = 13.3 ± 0.7 days). Fluorescent microsphere injections are described in the Supplemental Experimental Procedures.

In Vitro Slice Preparation

Acute thalamocortical brain slices (300 μ m thick) containing primary somatosensory (barrel) cortex were prepared from mice (between postnatal days 15 and 64) using methods described previously (Agmon and Connors, 1991; Crandall et al., 2015). In some cases, acute brain slices were cut in the coronal plane or at 45 degrees to the midline. Briefly, mice were deeply anesthetized via inhalation of isoflurane before being decapitated. Brains were quickly removed and placed in a cold ($\sim 4^\circ\text{C}$) oxygenated (95% O_2 , 5% CO_2) cutting solution containing (in mM): 3 KCl, 1.25 NaH_2PO_4 , 10 MgSO_4 , 0.5 CaCl_2 , 26 NaHCO_3 , 10 glucose, and 234 sucrose. Brain slices were cut using a vibrating tissue slicer (Leica VT1000) and then transferred to an incubation chamber filled with warm (32°C) oxygenated artificial cerebrospinal fluid (ACSF) containing (in mM): 126 NaCl, 3 KCl, 1.25 NaH_2PO_4 , 2 MgSO_4 , 2 CaCl_2 , 26 NaHCO_3 , and 10 glucose. Slices were maintained at 32°C for 20 min and then at room temperature for an additional 40–60 min before recording.

In Vitro Recordings and Data Acquisition

The ages of mice used for electrophysiological experiments ranged from postnatal day 20 to 33. For recordings, individual brain slices were transferred to a submersion recording chamber and bathed continually (2.5–3.0 mL/min) with warm ($32^\circ\text{C} \pm 1^\circ\text{C}$) oxygenated (95% O_2 , 5% CO_2) ACSF containing (in mM): 126 NaCl, 3 KCl, 1.25 NaH_2PO_4 , 2 MgSO_4 , 2.0 CaCl_2 , 26 NaHCO_3 , and 10 glucose. Neurons were visualized using infrared differential interference contrast (IR-DIC) optics and fluorescence microscopy with a Zeiss Axioskop microscope equipped with a video camera (Olympus XM10-IR). Pairs of L6 neurons (<200 μ m apart) were randomly selected from the upper half of the layer (that is, L6a). CT neurons were identified based on tdTomato expression in *Ntsr1: Ai9* and *Ntsr1: Ai14* mice or their direct ChR2-mediated response in *Ntsr1: Ai32* mice. CC neurons were identified based on their lack of tdTomato expression or direct ChR2-mediated response and verified post hoc based on their regular-spiking physiology (see Figures S3–S5). Whole-cell recordings were obtained using borosilicate glass patch pipettes (tip resistance between 3 and 6 $\text{M}\Omega$) containing a potassium-based internal solution (in mM): 130 K-gluconate, 4 KCl, 2 NaCl, 10 HEPES, 0.2 EGTA, 4 ATP-Mg, 0.3 guanosine triphosphate (GTP)-Tris, and 14 phosphocreatine-K (pH 7.25, 290 mOsm). All whole-cell recordings were corrected for a 14-mV liquid junction potential.

Electrophysiological data were acquired with an Axoclamp-2B (Axon Instruments) or MultiClamp 700B (Molecular Devices) microelectrode amplifier and then digitized at 20 kHz with a Digidata1322A (Axon Instruments) acquisition system and Clampex data acquisition software (Molecular Devices pClamp 10). All signals were low-pass-filtered at 10 kHz (current clamp) or

3 kHz (voltage clamp) prior to digitizing. During whole-cell recordings, the pipette capacitances were neutralized, and series resistances (typically 10–25 M Ω) were compensated online (100% for current clamp and 60%–80% for voltage clamp).

Photostimulation

ChR2 was optically excited using a high-power white light-emitting diode (LED) (Mightex LCS-5500-03-22) driven by a Mightex LED controller (SLC-AA02-US). Collimated light (in 1-ms flashes) was reflected through a single-edge dichroic beam-splitter (Semrock FF655-Di01) and then a high-magnification water immersion objective (Zeiss Achroplan 40 \times /0.75 W), resulting in a spot diameter of \sim 558 μ m and a maximum LED power at the focal plane of \sim 30 mW. In some experiments, collimated light was reflected through an Endow GFP filter set (Zeiss). For all L6a CT-CC cell paired recordings, photostimulation was directed at distal segments of thalamic axons within the barrel cortex with the light spot centered over the recorded cells. For photostimulation, pulse intensity was adjusted to \sim 3 \times the threshold for evoking an EPSP in L6 CC cells when held in current clamp at -84 mV. When recording ChR2-expressing neurons, the light was centered over the cell bodies.

Electrophysiological Data Analysis

Synaptic responses to photostimulation were measured from postsynaptic neurons recorded in whole-cell current clamp and voltage clamp. The area or amplitude of an evoked EPSP/EPSC was measured relative to a baseline before the stimulus (10 ms). The area of EPSCs was measured over the 10 ms immediately after the onset of the stimulus. Values were based on average responses to 3–20 stimuli (typically 10). Synaptic latencies were measured from stimulus onset to the average outward current onset. Details of analyses are described in the [Supplemental Experimental Procedures](#).

Histology, Microscopy, and Cell Counting

Details are described in the [Supplemental Experimental Procedures](#). Briefly, tissue for immunohistochemistry was prepared from acute brain slices, except for tissue cut in the tangential plane, which was prepared via transcardial perfusion, using methods described previously (Neske et al., 2015). Primary antibodies used were mouse monoclonal anti-NeuN (1:1,000; Millipore MAB377), guinea pig polyclonal anti-VGluT2 (1:12,000; Millipore AB2251), mouse monoclonal anti-Parvalbumin (1:2,000; Swant clone 235), and rabbit polyclonal anti-Somatostatin-14 (1:1,000; Bachem T4103).

Statistical Methods

All statistical comparisons were performed in OriginPro 9.0. No statistical methods were used to predetermine sample size, but our sample sizes are similar to those reported in previous studies (Crandall et al., 2015; Cruikshank et al., 2010). Unless stated in the results, no data points were excluded. The Shapiro-Wilk test was first applied to determine whether the data had been drawn from a normally distributed population, in which case parametric tests were used. If the assumption of normality was not valid, nonparametric tests were used. The following statistical tests were performed: t test, paired t test, Mann-Whitney U test, and paired Wilcoxon signed-rank test, as indicated in the [Results](#). All tests were two tailed. Data are presented as mean \pm SEM unless otherwise noted. Statistical significance was defined as $p < 0.05$. Experiments and data analysis were not performed blind to the conditions of the experiments.

SUPPLEMENTAL INFORMATION

Supplemental Information includes Supplemental Experimental Procedures, eight figures, and two tables and can be found with this article online at <https://doi.org/10.1016/j.celrep.2017.11.049>.

ACKNOWLEDGMENTS

We thank C.A. Deister, R. Martinez-Garcia, G.T. Neske, and A.U. Sugden for insightful comments and discussion. This research was supported by NIH grants K99-NS096108 (to S.R.C.), F32-NS084763 (to S.R.C.),

P20-GM103645 (to S.J.C.), R01-NS050434 (to B.W.C.), and R01-NS100016 (to S.J.C. and B.W.C.) and NSF award 1632738 (to B.W.C.).

AUTHOR CONTRIBUTIONS

S.R.C. and B.W.C. designed the study. S.R.C. conducted all experiments, imaging, and analyses except for histology. S.L.P. performed all histology. S.J.C. contributed to the imaging, writing, and design of the physiology experiments. S.R.C. and B.W.C. wrote the paper. All authors read and approved the final manuscript.

DECLARATION OF INTERESTS

The authors declare no competing interests.

Received: July 8, 2017

Revised: October 11, 2017

Accepted: November 14, 2017

Published: December 12, 2017

REFERENCES

- Agmon, A., and Connors, B.W. (1991). Thalamocortical responses of mouse somatosensory (barrel) cortex in vitro. *Neuroscience* 41, 365–379.
- Agmon, A., Yang, L.T., O'Dowd, D.K., and Jones, E.G. (1993). Organized growth of thalamocortical axons from the deep tier of terminations into layer IV of developing mouse barrel cortex. *J. Neurosci.* 13, 5365–5382.
- Ahissar, E., Sosnik, R., and Haidarliu, S. (2000). Transformation from temporal to rate coding in a somatosensory thalamocortical pathway. *Nature* 406, 302–306.
- Alloway, K.D. (2008). Information processing streams in rodent barrel cortex: the differential functions of barrel and septal circuits. *Cereb. Cortex* 18, 979–989.
- Alloway, K.D., Zhang, M., and Chakrabarti, S. (2004). Septal columns in rodent barrel cortex: functional circuits for modulating whisking behavior. *J. Comp. Neurol.* 480, 299–309.
- Andermann, M.L., and Moore, C.I. (2006). A somatotopic map of vibrissa motion direction within a barrel column. *Nat. Neurosci.* 9, 543–551.
- Audette, N.J., Urban-Ciecko, J., Matsushita, M., and Barth, A.L. (2017). P0m Thalamocortical Input Drives Layer-Specific Microcircuits in Somatosensory Cortex. *Cereb. Cortex* Mar 10, 1–17.
- Beierlein, M., and Connors, B.W. (2002). Short-term dynamics of thalamocortical and intracortical synapses onto layer 6 neurons in neocortex. *J. Neurophysiol.* 88, 1924–1932.
- Bokor, H., Acsády, L., and Deschênes, M. (2008). Vibrissa responses of thalamic cells that project to the septal columns of the barrel cortex and to the second somatosensory area. *J. Neurosci.* 28, 5169–5177.
- Bortone, D.S., Olsen, S.R., and Scanziani, M. (2014). Translaminar inhibitory cells recruited by layer 6 corticothalamic neurons suppress visual cortex. *Neuron* 82, 474–485.
- Briggs, F. (2010). Organizing principles of cortical layer 6. *Front. Neural Circuits* 4, 3.
- Briggs, F., Kiley, C.W., Callaway, E.M., and Usrey, W.M. (2016). Morphological Substrates for Parallel Streams of Corticogeniculate Feedback Originating in Both V1 and V2 of the Macaque Monkey. *Neuron* 90, 388–399.
- Brumberg, J.C., Hamzei-Sichani, F., and Yuste, R. (2003). Morphological and physiological characterization of layer VI corticofugal neurons of mouse primary visual cortex. *J. Neurophysiol.* 89, 2854–2867.
- Bureau, I., von Saint Paul, F., and Svoboda, K. (2006). Interdigitated paleomniscal and lemniscal pathways in the mouse barrel cortex. *PLoS Biol.* 4, e382.
- Chen, C.C., Abrams, S., Pinhas, A., and Brumberg, J.C. (2009). Morphological heterogeneity of layer VI neurons in mouse barrel cortex. *J. Comp. Neurol.* 512, 726–746.

- Chmielowska, J., Carvell, G.E., and Simons, D.J. (1989). Spatial organization of thalamocortical and corticothalamic projection systems in the rat Sml barrel cortex. *J. Comp. Neurol.* 285, 325–338.
- Constantinople, C.M., and Bruno, R.M. (2013). Deep cortical layers are activated directly by thalamus. *Science* 340, 1591–1594.
- Crandall, S.R., Cruikshank, S.J., and Connors, B.W. (2015). A corticothalamic switch: controlling the thalamus with dynamic synapses. *Neuron* 86, 768–782.
- Cruikshank, S.J., Lewis, T.J., and Connors, B.W. (2007). Synaptic basis for intense thalamocortical activation of feedforward inhibitory cells in neocortex. *Nat. Neurosci.* 10, 462–468.
- Cruikshank, S.J., Urabe, H., Nurmikko, A.V., and Connors, B.W. (2010). Pathway-specific feedforward circuits between thalamus and neocortex revealed by selective optical stimulation of axons. *Neuron* 65, 230–245.
- Denman, D.J., and Contreras, D. (2015). Complex Effects on In Vivo Visual Responses by Specific Projections from Mouse Cortical Layer 6 to Dorsal Lateral Geniculate Nucleus. *J. Neurosci.* 35, 9265–9280.
- Diamond, M.E., Armstrong-James, M., and Ebner, F.F. (1992). Somatic sensory responses in the rostral sector of the posterior group (POM) and in the ventral posterior medial nucleus (VPM) of the rat thalamus. *J. Comp. Neurol.* 318, 462–476.
- Diamond, M.E., von Heimendahl, M., Knutsen, P.M., Kleinfeld, D., and Ahissar, E. (2008). 'Where' and 'what' in the whisker sensorimotor system. *Nat. Rev. Neurosci.* 9, 601–612.
- Douglas, R.J., and Martin, K.A. (2004). Neuronal circuits of the neocortex. *Annu. Rev. Neurosci.* 27, 419–451.
- Feldman, D.E., and Brecht, M. (2005). Map plasticity in somatosensory cortex. *Science* 310, 810–815.
- Feldmeyer, D., Brecht, M., Helmchen, F., Petersen, C.C., Poulet, J.F., Staiger, J.F., Luhmann, H.J., and Schwarz, C. (2013). Barrel cortex function. *Prog. Neurobiol.* 103, 3–27.
- Fox, K. (2008). *Barrel cortex* (Cambridge Cambridge University Press).
- Furuta, T., Kaneko, T., and Deschênes, M. (2009). Septal neurons in barrel cortex derive their receptive field input from the lemniscal pathway. *J. Neurosci.* 29, 4089–4095.
- Gabernet, L., Jadhav, S.P., Feldman, D.E., Carandini, M., and Scanziani, M. (2005). Somatosensory integration controlled by dynamic thalamocortical feed-forward inhibition. *Neuron* 48, 315–327.
- Gong, S., Doughty, M., Harbaugh, C.R., Cummins, A., Hatten, M.E., Heintz, N., and Gerfen, C.R. (2007). Targeting Cre recombinase to specific neuron populations with bacterial artificial chromosome constructs. *J. Neurosci.* 27, 9817–9823.
- Groh, A., Bokor, H., Mease, R.A., Plattner, V.M., Hangya, B., Stroh, A., Deschenes, M., and Acsády, L. (2014). Convergence of cortical and sensory driver inputs on single thalamocortical cells. *Cereb. Cortex* 24, 3167–3179.
- Guo, W., Clause, A.R., Barth-Marón, A., and Polley, D.B. (2017). A Corticothalamic Circuit for Dynamic Switching between Feature Detection and Discrimination. *Neuron* 95, 180–194.e5.
- Harris, K.D., and Shepherd, G.M. (2015). The neocortical circuit: themes and variations. *Nat. Neurosci.* 18, 170–181.
- Herkenham, M. (1980). Laminar organization of thalamic projections to the rat neocortex. *Science* 207, 532–535.
- Horton, J.C., and Adams, D.L. (2005). The cortical column: a structure without a function. *Philos. Trans. R. Soc. Lond. B Biol. Sci.* 360, 837–862.
- Jacobson, S., and Trojanowski, J.Q. (1975). Corticothalamic neurons and thalamocortical terminal fields: an investigation in rat using horseradish peroxidase and autoradiography. *Brain Res.* 85, 385–401.
- Kerr, J.N., de Kock, C.P., Greenberg, D.S., Bruno, R.M., Sakmann, B., and Helmchen, F. (2007). Spatial organization of neuronal population responses in layer 2/3 of rat barrel cortex. *J. Neurosci.* 27, 13316–13328.
- Killackey, H.P., and Sherman, S.M. (2003). Corticothalamic projections from the rat primary somatosensory cortex. *J. Neurosci.* 23, 7381–7384.
- Kim, U., and Ebner, F.F. (1999). Barrels and septa: separate circuits in rat barrels field cortex. *J. Comp. Neurol.* 408, 489–505.
- Kim, J., Matney, C.J., Blankenship, A., Hestrin, S., and Brown, S.P. (2014). Layer 6 corticothalamic neurons activate a cortical output layer, layer 5a. *J. Neurosci.* 34, 9656–9664.
- Kinnischtzke, A.K., Fanselow, E.E., and Simons, D.J. (2016). Target-specific M1 inputs to infragranular S1 pyramidal neurons. *J. Neurophysiol.* 116, 1261–1274.
- Kumar, P., and Ohana, O. (2008). Inter- and intralaminar subcircuits of excitatory and inhibitory neurons in layer 6a of the rat barrel cortex. *J. Neurophysiol.* 100, 1909–1922.
- Lam, Y.W., and Sherman, S.M. (2010). Functional organization of the somatosensory cortical layer 6 feedback to the thalamus. *Cereb. Cortex* 20, 13–24.
- Lefort, S., Tómm, C., Floyd Sarria, J.C., and Petersen, C.C. (2009). The excitatory neuronal network of the C2 barrel column in mouse primary somatosensory cortex. *Neuron* 61, 301–316.
- Li, L., and Ebner, F.F. (2007). Cortical modulation of spatial and angular tuning maps in the rat thalamus. *J. Neurosci.* 27, 167–179.
- Lorente de Nó, R. (1938). Architectonics and structure of the cerebral cortex. In *Physiology of the Nervous System*, J.F. Fulton, ed. (London: Oxford University Press), pp. 291–327.
- Lu, S.M., and Lin, R.C. (1993). Thalamic afferents of the rat barrel cortex: a light- and electron-microscopic study using Phaseolus vulgaris leucoagglutinin as an anterograde tracer. *Somatosens. Mot. Res.* 10, 1–16.
- Ma, P.M. (1991). The barrelettes–architectonic vibrissal representations in the brainstem trigeminal complex of the mouse. I. Normal structural organization. *J. Comp. Neurol.* 309, 161–199.
- Madisen, L., Zwingman, T.A., Sunkin, S.M., Oh, S.W., Zariwala, H.A., Gu, H., Ng, L.L., Palmiter, R.D., Hawrylycz, M.J., Jones, A.R., et al. (2010). A robust and high-throughput Cre reporting and characterization system for the whole mouse brain. *Nat. Neurosci.* 13, 133–140.
- Madisen, L., Mao, T., Koch, H., Zhuo, J.M., Berenyi, A., Fujisawa, S., Hsu, Y.W., Garcia, A.J., 3rd, Gu, X., Zanella, S., et al. (2012). A toolbox of Cre-dependent optogenetic transgenic mice for light-induced activation and silencing. *Nat. Neurosci.* 15, 793–802.
- Mease, R.A., Krieger, P., and Groh, A. (2014). Cortical control of adaptation and sensory relay mode in the thalamus. *Proc. Natl. Acad. Sci. USA* 111, 6798–6803.
- Mercer, A., West, D.C., Morris, O.T., Kirchhecker, S., Kerkhoff, J.E., and Thomson, A.M. (2005). Excitatory connections made by presynaptic cortico-cortical pyramidal cells in layer 6 of the neocortex. *Cereb. Cortex* 15, 1485–1496.
- Mountcastle, V.B. (1957). Modality and topographic properties of single neurons of cat's somatic sensory cortex. *J. Neurophysiol.* 20, 408–434.
- Mountcastle, V.B. (1997). The columnar organization of the neocortex. *Brain* 120, 701–722.
- Narayanan, R.T., Egger, R., Johnson, A.S., Mansvelder, H.D., Sakmann, B., de Kock, C.P., and Oberlaender, M. (2015). Beyond Columnar Organization: Cell Type- and Target Layer-Specific Principles of Horizontal Axon Projection Patterns in Rat Vibrissal Cortex. *Cereb. Cortex* 25, 4450–4468.
- Neske, G.T., Patrick, S.L., and Connors, B.W. (2015). Contributions of diverse excitatory and inhibitory neurons to recurrent network activity in cerebral cortex. *J. Neurosci.* 35, 1089–1105.
- Oberlaender, M., de Kock, C.P., Bruno, R.M., Ramirez, A., Meyer, H.S., Dercksen, V.J., Helmstaedter, M., and Sakmann, B. (2012). Cell type-specific three-dimensional structure of thalamocortical circuits in a column of rat vibrissal cortex. *Cereb. Cortex* 22, 2375–2391.
- Olsen, S.R., Bortone, D.S., Adesnik, H., and Scanziani, M. (2012). Gain control by layer six in cortical circuits of vision. *Nature* 483, 47–52.
- Peteanu, L., Mao, T., Sternson, S.M., and Svoboda, K. (2009). The subcellular organization of neocortical excitatory connections. *Nature* 457, 1142–1145.

- Pierret, T., Lavallée, P., and Deschênes, M. (2000). Parallel streams for the relay of vibrissal information through thalamic barreloids. *J. Neurosci.* 20, 7455–7462.
- Shepherd, G.M., and Svoboda, K. (2005). Laminar and columnar organization of ascending excitatory projections to layer 2/3 pyramidal neurons in rat barrel cortex. *J. Neurosci.* 25, 5670–5679.
- Sherman, S.M. (2016). Thalamus plays a central role in ongoing cortical functioning. *Nat. Neurosci.* 19, 533–541.
- Simons, D.J. (1978). Response properties of vibrissa units in rat SI somatosensory neocortex. *J. Neurophysiol.* 41, 798–820.
- Staiger, J.F., Zilles, K., and Freund, T.F. (1996). Recurrent axon collaterals of corticothalamic projection neurons in rat primary somatosensory cortex contribute to excitatory and inhibitory feedback-loops. *Anat. Embryol. (Berl.)* 194, 533–543.
- Swadlow, H.A. (1989). Efferent neurons and suspected interneurons in S-1 vibrissa cortex of the awake rabbit: receptive fields and axonal properties. *J. Neurophysiol.* 62, 288–308.
- Temereanca, S., and Simons, D.J. (2004). Functional topography of corticothalamic feedback enhances thalamic spatial response tuning in the somatosensory whisker/barrel system. *Neuron* 41, 639–651.
- Thompson, A.D., Picard, N., Min, L., Fagiolini, M., and Chen, C. (2016). Cortical Feedback Regulates Feedforward Retinogeniculate Refinement. *Neuron* 91, 1021–1033.
- Thomson, A.M. (2010). Neocortical layer 6, a review. *Front. Neuroanat.* 4, 13.
- Tremblay, R., Lee, S., and Rudy, B. (2016). GABAergic Interneurons in the Neocortex: From Cellular Properties to Circuits. *Neuron* 91, 260–292.
- Van Der Loos, H. (1976). Barreloids in mouse somatosensory thalamus. *Neurosci. Lett.* 2, 1–6.
- Vélez-Fort, M., Rousseau, C.V., Niedworok, C.J., Wickersham, I.R., Rancz, E.A., Brown, A.P., Strom, M., and Margrie, T.W. (2014). The stimulus selectivity and connectivity of layer six principal cells reveals cortical microcircuits underlying visual processing. *Neuron* 83, 1431–1443.
- Welker, C., and Woolsey, T.A. (1974). Structure of layer IV in the somatosensory neocortex of the rat: description and comparison with the mouse. *J. Comp. Neurol.* 158, 437–453.
- Wimmer, V.C., Bruno, R.M., de Kock, C.P., Kuner, T., and Sakmann, B. (2010). Dimensions of a projection column and architecture of VPM and POm axons in rat vibrissal cortex. *Cereb. Cortex* 20, 2265–2276.
- Wise, S.P., and Jones, E.G. (1977). Cells of origin and terminal distribution of descending projections of the rat somatic sensory cortex. *J. Comp. Neurol.* 175, 129–157.
- Woolsey, T.A., and Van der Loos, H. (1970). The structural organization of layer IV in the somatosensory region (SI) of mouse cerebral cortex. The description of a cortical field composed of discrete cytoarchitectonic units. *Brain Res.* 17, 205–242.
- Yamawaki, N., and Shepherd, G.M. (2015). Synaptic circuit organization of motor corticothalamic neurons. *J. Neurosci.* 35, 2293–2307.
- Yang, Q., Chen, C.C., Ramos, R.L., Katz, E., Keller, A., and Brumberg, J.C. (2014). Intrinsic properties of and thalamocortical inputs onto identified corticothalamic-VPM neurons. *Somatosens. Mot. Res.* 31, 78–93.
- Yu, C., Derdikman, D., Haidarliu, S., and Ahissar, E. (2006). Parallel thalamic pathways for whisking and touch signals in the rat. *PLoS Biol.* 4, e124.
- Zhang, Z.W., and Deschênes, M. (1997). Intracortical axonal projections of lamina VI cells of the primary somatosensory cortex in the rat: a single-cell labeling study. *J. Neurosci.* 17, 6365–6379.